



This is a repository copy of *Quantitative characterization of machining-induced white layers in Ti-6Al-4V*.

White Rose Research Online URL for this paper:  
<http://eprints.whiterose.ac.uk/149313/>

Version: Accepted Version

---

**Article:**

Brown, M. [orcid.org/0000-0002-0937-9139](https://orcid.org/0000-0002-0937-9139), Crawforth, P., M'Saoubi, R. et al. (4 more authors) (2019) Quantitative characterization of machining-induced white layers in Ti-6Al-4V. *Materials Science and Engineering: A*, 764. 138220. ISSN 0921-5093

<https://doi.org/10.1016/j.msea.2019.138220>

---

Article available under the terms of the CC-BY-NC-ND licence  
(<https://creativecommons.org/licenses/by-nc-nd/4.0/>).

**Reuse**

This article is distributed under the terms of the Creative Commons Attribution-NonCommercial-NoDerivs (CC BY-NC-ND) licence. This licence only allows you to download this work and share it with others as long as you credit the authors, but you can't change the article in any way or use it commercially. More information and the full terms of the licence here: <https://creativecommons.org/licenses/>

**Takedown**

If you consider content in White Rose Research Online to be in breach of UK law, please notify us by emailing [eprints@whiterose.ac.uk](mailto:eprints@whiterose.ac.uk) including the URL of the record and the reason for the withdrawal request.



[eprints@whiterose.ac.uk](mailto:eprints@whiterose.ac.uk)  
<https://eprints.whiterose.ac.uk/>

# Quantitative Characterization of Machining-Induced White Layers in Ti-6Al-4V

M.Brown<sup>a,f</sup>, P.Crawforth<sup>b</sup>, R.M'Saoubi<sup>c</sup>, T.Larsson<sup>c</sup>, B.Wynne<sup>d</sup>, A.Mantle<sup>e</sup>,  
H.Ghadbeigi<sup>f</sup>

<sup>a</sup> Industrial Doctoral Centre in Machining Science, Advanced Manufacturing Research Centre with Boeing, University of Sheffield, Rotherham, S60 5TZ, UK

<sup>b</sup> Advanced Manufacturing Research Centre with Boeing, University of Sheffield, Rotherham, S60 5TZ, UK

<sup>c</sup> Materials & Technology development, Seco Tools AB, SE73782 Fagersta, Sweden

<sup>d</sup> The University of Sheffield, Department of Materials Science and Engineering, Sir Robert Hadfield Building, Mappin Street, S1 3JD, Sheffield, UK

<sup>e</sup> Manufacturing Technology, Rolls-Royce PLC, Derby, UK

<sup>f</sup> The University of Sheffield, Department of Mechanical Engineering, Sir Frederick Mappin Building, Mappin Street, S1 3JD, Sheffield, UK

## Abstract

Machining-induced white layers can affect the functional performance of engineered components, due to the resulting mechanical and microstructural properties.

Destructive inspection methods such as cross-sectional microscopy are typically used to identify white layers, however, these methods are inherently costly and time-consuming. It is, therefore, desirable to detect this anomalous surface feature using non-destructive methods which requires improved knowledge around the characteristics of white layers. The present paper reports on the characterization of white layers formed during machining of Ti-6Al-4V, to aid future development of a reliable non-destructive assessment method. The microstructure of the material in the white layer was found to have a basal (0002)  $\alpha$ -hexagonal close packed texture

and there was no evidence of an  $\alpha \rightarrow \beta$  phase transformation during white layer formation. The white layer has a highly refined grain structure with an increased nanohardness of up to 15% compared with the bulk material. It is proposed that white layers in Ti-6Al-4V are formed by continuous dynamic recrystallization driven by severe plastic deformation during machining. According to the measured micro-mechanical properties of the white layer, suitable non-destructive testing methods are suggested for the detection of this surface feature.

Keywords: White layer; Surface integrity; Titanium; Machining; Characterization

## **1 Introduction**

Surface integrity (SI) has been defined by Koster et al. [1] as the altered condition of a surface post-machining. Within SI features, white layers are one of the most critical aspects as they can significantly affect a component's performance and expected lifetime in service. White layers are typically identified as the regions in which the microstructure is indistinguishable at a resolution that resolves the bulk [2]. These usually appear as a white coloured layer in a cross-sectional micrograph of the near-surface of an etched metallic sample. White layers are named as such due to their appearance under optical light microscopy. Chou and Evans [3] attributed this white appearance to an increased resistance to conventional etchants, which prevents the white layer structure being revealed during optical microscopy. By contrast, Akcan et al. [4] proposed that it was due to the scattering of light from the ultra-fine grains in the white layer (<100 nm) as a consequence of the comparatively large wavelength of visible light.

White layers have been shown to form during different machining operations such as milling [5], drilling [6], turning [7], grinding [8], broaching [9] and electrical discharge machining [10]. They have also been observed in worn rail tracks [11], components made by high-velocity shaping and forming processes [12] and samples subjected to ballistic impact loads [13]. Machining induced white layers are more typically formed when cutting difficult-to-machine alloys. Poulachon et al. [14] have shown that the white layers can be formed on most ferrous alloys used in aero-engines, whilst Herbert et al. [6] and Edkins et al. [15] have identified that nickel superalloys and titanium alloys are also prone to the formation of this anomalous SI feature.

Akan et al. [4] have shown, using destructive characterization methods, that the white layer has a higher hardness relative to the bulk material in steel. Barry and Byrne [16] reported that white layers are composed of ultra-fine grains and Smith et al. [17] measured extremes of near-surface residual stresses when a white layer was present on a surface. Herbert et al. [18] reported that the presence of a white layer on the machined surface of a nickel superalloy can reduce the low-cycle fatigue life by as much as 30 times in extreme cases. The thickness of white layers typically ranges between several microns, as measured by Ramesh et al. [7], to several tens of microns, as reported by Wusatowska-Sarnek et al. [19].

Griffiths [20] outlined three mechanisms for the formation of a white layer, (a) phase transformation (PT) (b) severe plastic deformation (SPD) with dynamic recrystallization and (c) chemical surface reactions. In difficult-to-machine alloys, such as high-strength steels, white layers have been shown to form by the PT mechanism, as identified by Ramesh et al. [7], or the SPD mechanism, as observed by Hosseini et al. [21]. However, recent research by Xu et al. [22] has shown that white layers can form due to a combination of both.

For the white layers formed by the PT mechanism in steels, Barry and Byrne [16] reported that there is a higher retained austenite concentration than in the bulk of the material. Barry and Byrne [16] concluded this to be a result of the temperature rise during machining exceeding the austenitization limit. Under subsequent rapid cooling, which results in a martensitic transformation, a proportion of austenite was untransformed. Poulachon [14] identified that dynamic recrystallization, driven by SPD, also results in a white layer with an ultra-fine grained microstructure in steels, however, in this mechanism, there is no change in phase or chemical composition. In surfaces with an SPD-type white layer, there is typically a swept grain region beneath, visible as a distorted layer in optical micrographs. This region consists of highly distorted material forming deformation bands in the direction of machining, as shown by Herbert et al. [23].

In their study of high speed machining (HSM) of titanium, Xu et al. [22] generated surfaces with a white layer. It proposed that the white layer formed due to continuous dynamic recrystallization under high strain rate. Dislocation slip alongside  $\{10\bar{1}1\}$  and  $\{10\bar{1}2\}$  twinning were thought to facilitate the deformation in the white layer. Xu et al. [22] also identified  $\beta$  precipitation under the strain and high temperatures experienced during HSM. It was proposed that these precipitates prevented grain growth in the recrystallized white layer grains by pinning them. The formation mechanism proposed by Xu et al. [22] is, therefore, a mixture of SPD and phase transformation, with the appearance  $\beta$  precipitates indicating that one mechanism is not always solely responsible for white layer formation. In the adiabatic shear band of a titanium chip, which can be considered to be a form of a white layer in the chip due to the physical similarities, Wan et al. [24] measured, through x-ray diffraction, that the  $\alpha''$  phase was present. This indicates that the temperatures during cutting

were sufficient for an  $\alpha \rightarrow \beta$  transformation followed by a  $\beta \rightarrow \alpha$  transformation under cooling.

Bushlya et al. [25] reported that, during the machining of nickel-based superalloys, higher cutting speeds and flank wear levels result in a greater level of white layer formation. Machining with worn tools results in greater shear deformation of the workpiece, as shown by Zhou et al. [26], where the extent of deformation and surface damage are proportional to the level of tool wear. Fang-Yuan et al. [27] and Xu et al. [22] identified that high cutting speeds increase the tendency for white layer formation through the PT mechanism in steels and a mixed SPD and PT mechanism in titanium respectively. Higher cutting speeds encourage phase transformation due to the greater heat generation in the workpiece.

The drive for higher metal removal rates in industry, to increase production rates, has resulted in the adoption of higher cutting speeds [28]. Therefore, it is expected that the problem of white layer formation during the machining of difficult-to-machine aero-engine alloys will become increasingly relevant in modern machining processes.

Cross-sectional microscopy, as a method for identifying white layers, is inherently costly, in terms of parts sacrificed, and time-consuming, due to the numerous process steps involved in preparing metallographic samples. Therefore, there is a high demand to detect any possible formed white layer using non-destructive testing (NDT) techniques. Brown et al. [29] highlighted the techniques most suited to white layer detection in their review on the subject where key physical properties required for the development of non-destructive testing (NDT) methods for white layers were also identified. These properties include microstructure, composition, crystallographic texture, nanohardness and residual stress state. White layers

formed in steels [7], and more recently nickel superalloys [6], have been widely characterized, in terms of the key physical properties highlighted by Brown et al. [29]. In contrast, there is very limited knowledge on white layers formed in titanium alloys, despite the widespread use of these alloys in aerospace applications. Edkins et al. [15] only identified the presence of a white layer in Ti-6Al-4V through microscopy, with no characterization undertaken.

This paper, therefore, aims to quantify key properties of machining-induced white layers in Ti-6Al-4V, the most common titanium alloy, to guide future development of an NDT method for detection of this anomalous surface feature.

## **2 Experimental methods**

### **2.1 Outline of the study**

Surfaces with and without white layers had to first be generated in order to characterize this SI feature. Since tool wear was identified in the previous section as a significant contributing factor in white layer formation, milling operations using cutting tools having controlled levels of artificial flank wear were designed and undertaken to generate the required surfaces. The produced samples were then characterized using a range of techniques to determine the key properties of the generated white layers.

### **2.2 Material**

Mill-annealed Ti-6Al-4V was provided for the milling trials by Rolls-Royce plc as slabs with dimensions of 200 x 66 x 19 mm cut from the same cross-rolled plate by wire electrical discharge machining. The specimens were sectioned so that their longest axis lay parallel to the final roll direction (FRD), as shown in Figure 1 (a), wherein the cross-rolled direction (CRD) is perpendicular to the FRD. The

microstructure of the as-received material consisted of 20-30  $\mu\text{m}$  sized primary  $\alpha$ -grains with residual grain boundary  $\beta$ , as highlighted in Figure 1 (b). The volume fraction of the residual  $\beta$ -phase was estimated to be 15-20% using particle analysis techniques on Fiji ImageJ software [30].

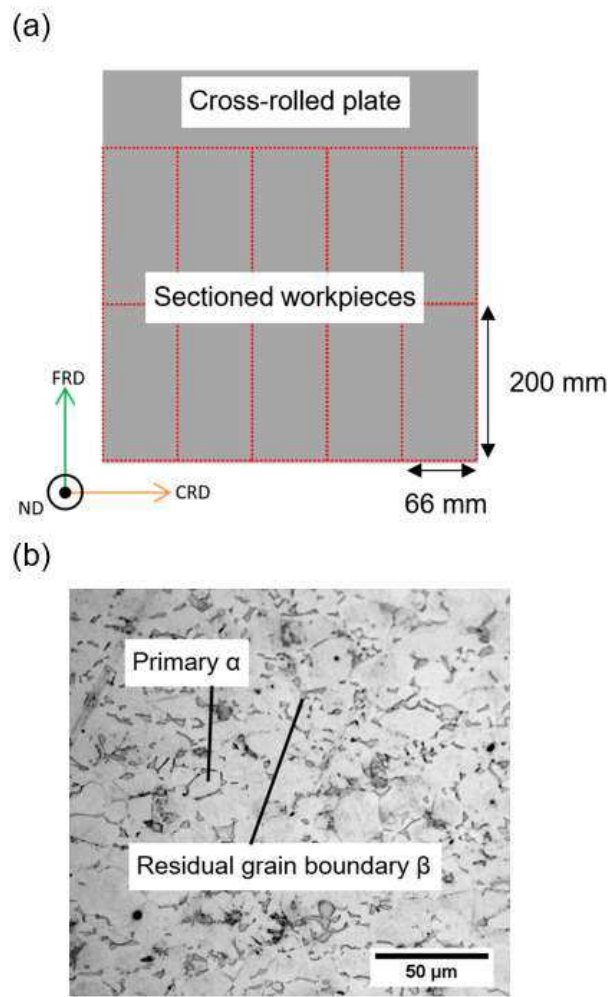


Figure 1 – Schematic of the workpieces obtained from a cross-rolled plate (a) and a cross-sectional micrograph of the as-received material (b). (single column)

### 2.3 White layer generation

Single-point milling was carried out using a Mori-Seiki Nv5000 $\alpha$ 1 vertical machining centre with a Seco Tools shoulder milling cutter (R217.69-2020.0-12-2AN) and coated tungsten carbide inserts (XOEX120408R-M07 MS2050). A Kistler 9139AA multicomponent dynamometer was used to measure the forces during cutting at a

sampling frequency of 1000 Hz. A number of the inserts were ground on their clearance face to result in two different levels of flank wear ( $VB = 0.5$  mm and  $0.85$  mm), as shown in Figure 2 (a). It should be noted that the wear on the inserts was beyond the  $0.2$  mm average flank wear criterion typically used to define tool-life in industry, however, the inserts were used exclusively to generate samples with thick white layers. After grinding, the inserts were re-honed to provide a nose radius of  $800\ \mu\text{m}$  and a cutting edge radius of approximately  $30\ \mu\text{m}$ , measured using an Alicona InfiniteFocusSL microscope.

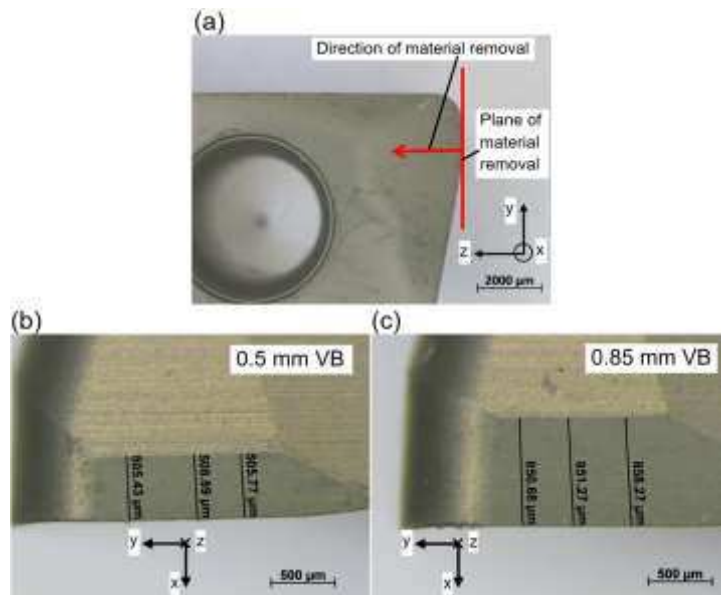


Figure 2 – Micrographs of the cutting inserts: The location and direction of the material removal from the grinding process used to prepare "worn" inserts (a). The two different levels of flank wear on the inserts (b,c). (single column)

A range of cutting speeds ( $20$ - $200$  m/min) were imposed in an attempt to achieve machining conditions with dominant thermal effects (higher speeds) and mechanical effects (lower speed) on the workpiece material. These correspond to an increased likelihood of generating white layers through the PT and SPD mechanisms, respectively, as reported by Hosseini et al. [10]. Slower cutting speeds were necessary when machining with the ground inserts to reduce the failure rate of the

inserts under the high temperatures and forces caused by the frictional contact of the worn regions with the workpiece. Figure 3 shows a schematic of the designed cutting setup wherein the feed rate and radial depth of cut were kept constant at 0.06 mm/tooth and 16 mm, respectively, and two levels of 0.5mm and 2mm were implemented for the axial engagement. The milling trials with fresh cutting inserts were also conducted under both dry and wet conditions, wherein the coolant was applied under a conventional flood cooling regime, to enhance and suppress thermal effects respectively.

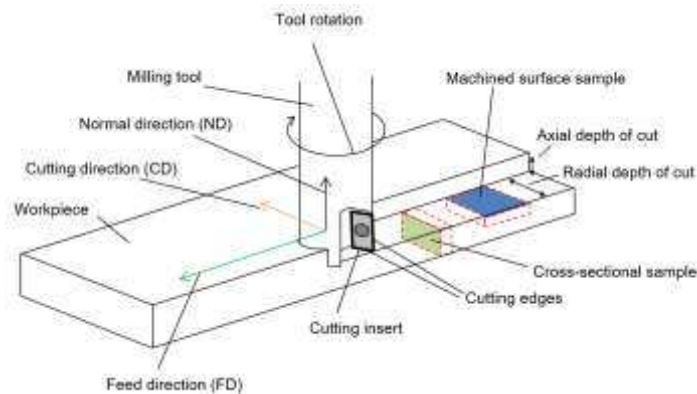


Figure 3 - Schematic of the cutting operation highlighting the orientation of samples sectioned from the machined workpiece for surface characterization, as well as the directions referred to in the XRD pole figures and residual stress measurements. (single column)

## 2.4 Characterization

### 2.4.1 Microscopy

A number of samples, encompassing the full range of cutting conditions were sectioned, as shown in Figure 3, to allow characterization of the surface and sub-surface properties of the generated machined sections. A small selection of the sectioned samples were heated at 700 °C for 2 hours in a vacuum furnace, after initial micrograph analysis, to enlarge the microstructure in the white layers without exceeding the  $\beta$ -transus temperature. Standard metallurgical preparation procedures

were followed to prepare samples for all microscopy. Mechanically polished samples, at mirror finish condition, were etched using Kroll's reagent until the mirror finish on the samples changed to cloudy in appearance.

An Olympus BX51 microscope was used to capture optical micrographs of etched surfaces at 500x magnification, for consistency with industry inspection methods [2].

The micrographs, as shown in Figure 4 (a), were decomposed into three distinct sections including, I) the white layer, II) the deformed region beneath, termed here the swept grain region, and III) the bulk, according to the criteria given by Puerta-Velásquez et al. [31]. The white layer thickness was calculated as an average of 15 measurements from 3 micrographs along each sample, as shown in Figure 4 (b).

Due to the curved tool path in milling, the direction of grain distortion changes across the width of the machined shoulder, illustrated by the radial depth of cut direction in Figure 3. Therefore, all the swept grain depth measurements were obtained from an average of 10 measurements at two locations near the centre of the cross-sectional sample, as shown in Figure 4 (b). At these locations, the tool pass direction and therefore the grain distortion was in the plane of the image. An inspect F50 field emission gun (FEG) scanning electron microscope (SEM) was used to investigate the microstructure within the white layer in polished and un-etched cross-sectional samples.

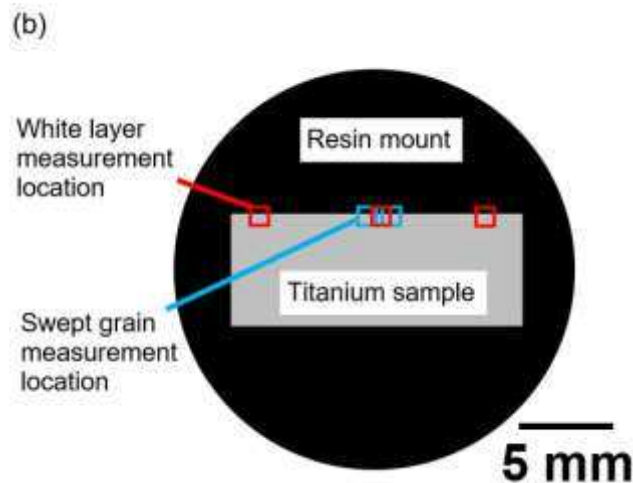
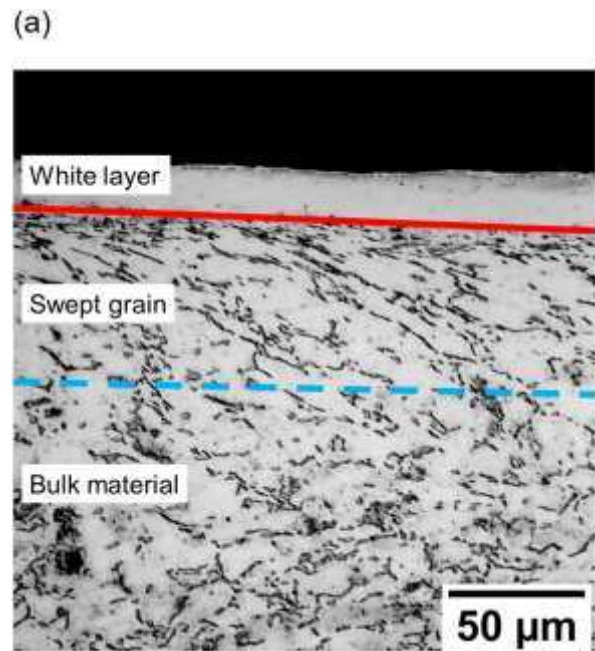


Figure 4 – (a) A representative optical micrograph of an etched sample in which measurements were carried out to define the thickness of the white layer and the swept grain depth. The white layer thickness and the swept grain depth are highlighted by the solid and dashed lines respectively. (b) A schematic highlighting the locations of the optical microscopy measurements in a cross-sectional sample. (single column)

#### 2.4.2 Nanoindentation measurements

To determine the hardness and elastic modulus variation below the machined surface, cross-sectional profiles were obtained using a Triboscope nanoindenter, through the Oliver & Pharr [32] method. A 5000  $\mu\text{N}$  load was applied with a Berkovich indenter on the mirror-polished samples over an 11 x 5 indentation array

that was 50  $\mu\text{m}$  x 25  $\mu\text{m}$  in size with eleven indentations in the depth direction, as shown in Figure 5. Hardness and elastic modulus values were averaged for each of the five indentations at every depth interval. An atomic force microscope was used to position the indenter adjacent to the machined surface. Additional indentations to investigate the effect of crystallographic orientation on hardness and elastic modulus in the white layer were undertaken using a 4 x 4 array on machined surface samples and averaged to obtain a single value. A bulk material hardness was obtained by averaging indentations from a 4 x 4 array in the as-received material. In all indentations, the first indentation beneath the surface, as well as adjacent indentations, were kept a distance of three indentation diameters apart, as defined in ASTM E384 [33]. The indenter material constants,  $E_i$  and  $\nu_i$ , were taken as 1141 GPa and 0.07 respectively. A value of 0.34 was used as the Poisson's ratio for the Ti-6Al-4V samples based on the median of the range of values outlined by Welsch et al. [34].

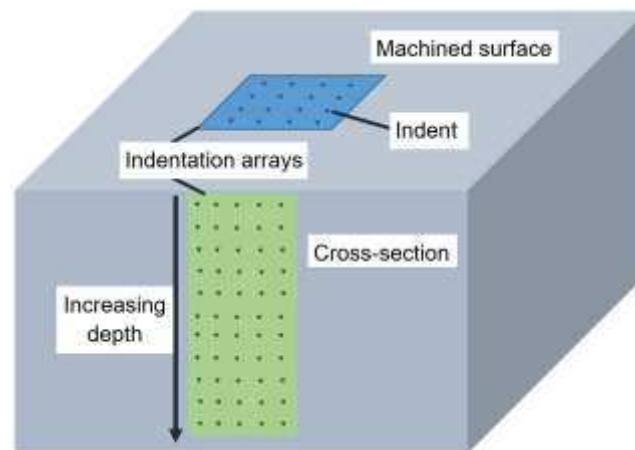


Figure 5 – A schematic outlining the location of the nanoindentation measurements. (single column)

### 2.4.3 Phase analysis

Microstructural phases of the machined surfaces were analyzed using a PANalytical X'Pert<sup>3</sup> X-ray diffractometer. The measurements were conducted at room

temperature on samples with and without white layers as well as an example of the as-received material. Copper  $K\alpha$  x-rays were used and the penetration depths, for 90% beam attenuation, were calculated to be between 4.3  $\mu\text{m}$  and 9.2  $\mu\text{m}$ , using AbsorbDX software [35], for the range of imposed diffraction angles, 35°- 80°. The XRD measurements were carried out over an area of approximately 8 mm x 4 mm on the machined surfaces. PDF-4+ Sleve+ software [36] was used to fit empirical phase data from the International Centre for Diffraction Data [37] to the diffraction patterns using the indexing program.

A further test, using XRD, was carried out in the phase analysis configuration for angles between 36° and 43°, to investigate the potential for detecting white layers non-destructively. From the measured diffraction pattern, the intensity ratio, defined here as the ratio between the intensity of the  $\alpha(0002)$  peak and the  $\alpha(10\bar{1}1)$ , was calculated and used as a quantitative measure to distinguish between surfaces.

#### **2.4.4 Crystallographic texture analysis**

To investigate the effects of white layer formation on the crystallographic texture of the material, a Bruker D8 Advance diffractometer with copper  $K\alpha$  radiation was used to obtain x-ray pole figure maps of machined surfaces as well as the as-received material. The crystallographic textures were measured for diffraction angles in a range of 34°- 44° which corresponds to a penetration depth of approximately 4.2  $\mu\text{m}$  - 5.4  $\mu\text{m}$ . The area under investigation in each case was 5 mm x 2 mm. For two machined surface samples, the white layer was mechanically polished away before pole figure measurements took place, to reveal the swept grain material beneath and allow investigation of the texture of this region. Material removal was quantified using a digital micrometer and cross-referenced against the known white layer thickness in each sample from microscopy, to ensure the white layer had been removed. A

reference measurement was taken from a powder sample to correct the results for defocusing and background intensity. MTEX, as described by Bachmann et al. [38], was used to calculate the orientation distribution functions (ODF) from the corrected data and then plot recalculated pole figures.

#### **2.4.5 Residual stress measurements**

Residual stress profiles were measured using a Proto iXRD portable diffractometer with a copper K $\alpha$  x-ray tube. In-depth profile measurements were achieved through successive material removal using the electropolishing technique. The  $\sin^2(\psi)$  method with 6 tilt angles ( $\psi$ ) between  $-19^\circ$  and  $+19^\circ$ , was used to measure crystal lattice strain and, through calculation, residual stress in the feed and cutting directions, as described by Cullity and Stock [39]. The  $\alpha(21\bar{3}3)$  peak was chosen for the measurements due to its high Bragg angle (approximately  $140^\circ$ ) [37] as Fitzpatrick et al. [40] have shown that higher angles result in larger changes in diffraction angle for a given change in lattice spacing. Elastic constants used in the stress calculation were  $S_1 = -2.97 \times 10^{-6} \text{ MPa}^{-1}$  and  $S_2/2 = 11.89 \times 10^{-6} \text{ MPa}^{-1}$ , which correspond to an Elastic modulus of 112.1 GPa and a Poisson's ratio of 0.33. Flat plate corrections were applied to account for the stress relaxation effect of layer removal, as outlined by Sikarskie [41]. In addition to stress measurements, peak broadening was also obtained for the  $\alpha(21\bar{3}3)$  peak in each sample. The peak broadening was taken as the full width of the peak at half of the maximum intensity.

### **3 Results**

#### **3.1 Microstructural morphology of the white layer**

The results from the quantitative analysis of cross-sectional micrographs taken from various samples are shown in Table 1, together with the associated cutting

conditions for the generation of each surface. It can be seen that white layers were only formed when machining with a worn insert and there is high uncertainty in the measured thickness of the white layers due to the variation in measurements at different locations across the machined surface.

Table 1 – Metallurgical analysis of selected samples. (single column)

Sample	White layer thickness ( $\mu\text{m}$ )	Depth of swept grain ( $\mu\text{m}$ )	Cutting speed (m/min)	Ground flank wear (mm)	Axial depth of cut (mm)
Unmachined	0	0	n/a	n/a	n/a
1	0	6.8 ( $\pm 1.1$ )	60	0	2.0
2	0	5.1 ( $\pm 0.9$ )	20	0	2.0
3	0	3.5 ( $\pm 0.8$ )	200	0	0.5
4	0	2.4 ( $\pm 0.5$ )	40	0	0.5
5	8.0 ( $\pm 1.7$ )	59.9 ( $\pm 7.0$ )	20	0.85	2.0
6	10.4 ( $\pm 4.5$ )	85.0 ( $\pm 8.6$ )	20	0.85	2.0
7	7.9 ( $\pm 3.8$ )	58.5 ( $\pm 19.3$ )	80	0.5	0.5
8	16.4 ( $\pm 3.9$ )	70.8 ( $\pm 13.4$ )	40	0.5	2.0
9	9.3 ( $\pm 4.3$ )	107.5 ( $\pm 9.6$ )	80	0.5	0.5
10	12.4 ( $\pm 3.1$ )	117.1 ( $\pm 18.5$ )	40	0.5	2.0
11	7.5 ( $\pm 3.5$ )	85.0 ( $\pm 21.4$ )	40	0.85	2.0

Figure 6 (a) shows a 10,000x magnification FEG-SEM micrographs of the white layer from sample 9, formed by machining with a 0.5 mm worn insert, in which the white layer and swept grain regions are highlighted. The higher magnification micrograph in Figure 6 (b), shows the difficult-to-resolve ultrafine microstructure in the white layer which is at the limit of the resolution capability of the equipment. The microstructure of the white layer is more easily resolved in Figure 6 (c), at the transition between the white layer and swept grain regions. It can be seen that the white layer, in this location, consists of nano-scale equiaxed grains with an average grain size of less than 200 nm, measured using the Heyn linear intercept method as described in ASTM E112 [42]. This grain size contrasts considerably with the 20-30  $\mu\text{m}$   $\alpha$ -phase grain size and the elongated grain boundary- $\beta$  in the bulk microstructure visible in the optical micrograph of Figure 1 (a). In the white layer, any retained- $\beta$  is

indistinguishable from the primary- $\alpha$ , whereas, in the transition and swept grain regions, Figure 6 (c) and (d) respectively, the  $\beta$ -phase can be resolved due to atomic number contrast in the micrograph. The microstructure immediately below the white layer, Figure 6 (d) shows that the grain sizes are increasing in the swept grain region immediately below the white layer, but they are still smaller than 500 nm.

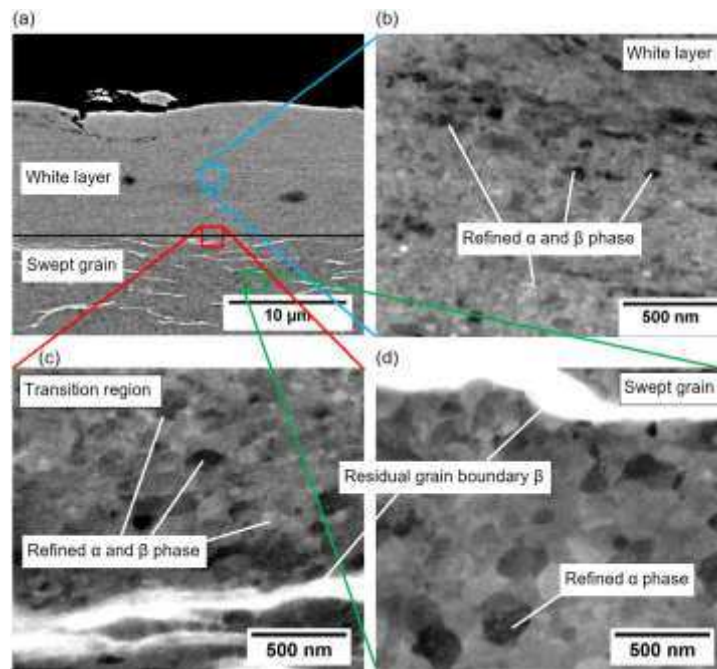


Figure 6 – Cross-sectional backscattered electron SEM images of un-etched sample 9 sectioned perpendicular to the feed direction showing the white layer and the swept grain region at 10,000 x (a), a higher magnification (160,000 x) image of the white layer (b), the transition region between white layer and swept grain (c) and the swept grain region (d). (single column)

The microstructure of a machined surface with a white layer which has been heat-treated in a vacuum furnace at 700 °C for 2 hours, is presented in Figure 7. It can be seen that this heat treatment has resulted in grain growth within the white layer region. It is apparent that the white layer is composed of both the  $\alpha$  and  $\beta$ -phases and the  $\beta$ -phase is found at the  $\alpha$ -grain boundaries.

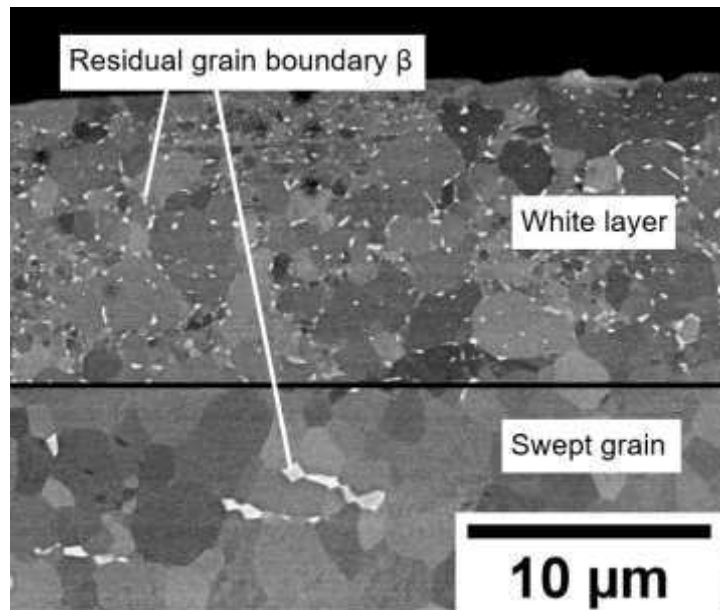


Figure 7 – Cross-sectional backscattered SEM micrograph of un-etched sample 6 which had been heat-treated below the  $\beta$ -transus to result in grain growth. (single column)

### 3.2 Phase and chemical composition of the white layer

XRD patterns for machined surfaces and an unmachined surface are shown in Figure 8, wherein only peaks corresponding to the  $\alpha$ -phase can be resolved for all surfaces examined. The absence of  $\beta$ -phase peaks is due to the small (15-20%) volume fraction of the  $\beta$ -phase, even in the as-received material, in addition to masking of the  $\beta(110)$  peak by the  $\alpha(0002)$  peak. However, the larger  $\alpha(0002)$  peak for a surface with a white layer (sample 8) cannot be correlated to an increase in the underlying  $\beta(110)$  peak as there is no concurrent appearance of the  $\beta(200)$  peak at  $56^\circ$  or the  $\beta(211)$  at  $70^\circ$ .

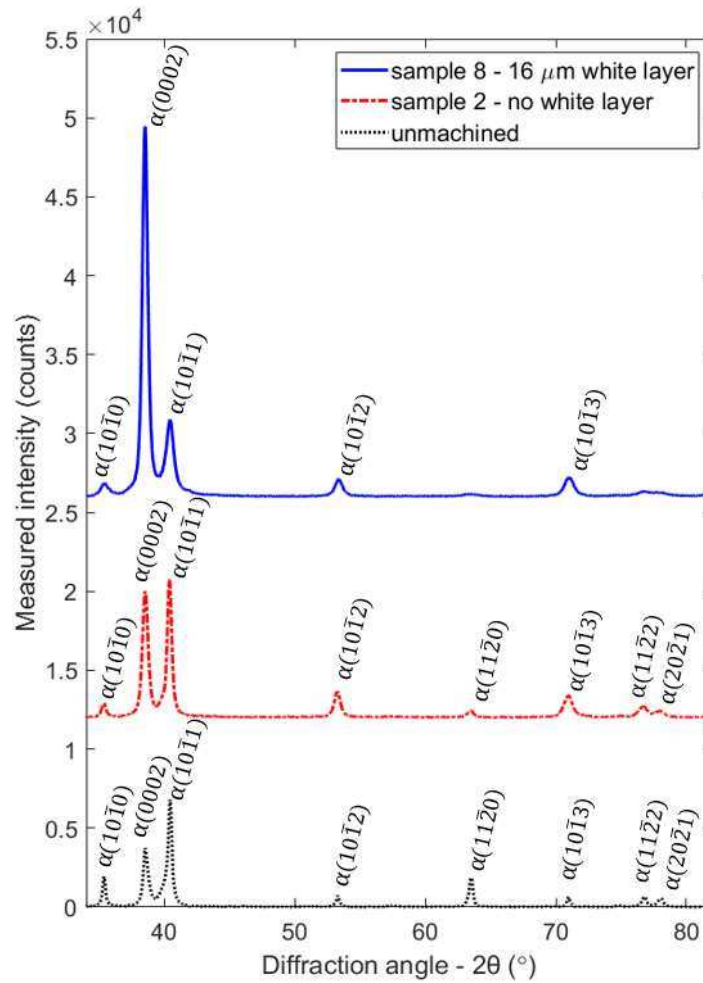


Figure 8 – XRD patterns for a machined surface with a 20 μm white layer (top), a machined surface with no white layer (middle) and an unmachined surface for reference (bottom). (single column)

### 3.3 Crystallographic texture of the white layer

XRD pole figures, shown in Figure 9 (a) and (b), highlight the crystallographic texture of the as-received material at depths corresponding to the axial depths of cut used during the machining trials. It can be seen that the basal (0002) poles are preferentially orientated in the final rolling direction (FRD) and the cross-rolled direction (CRD) in the as-received material.

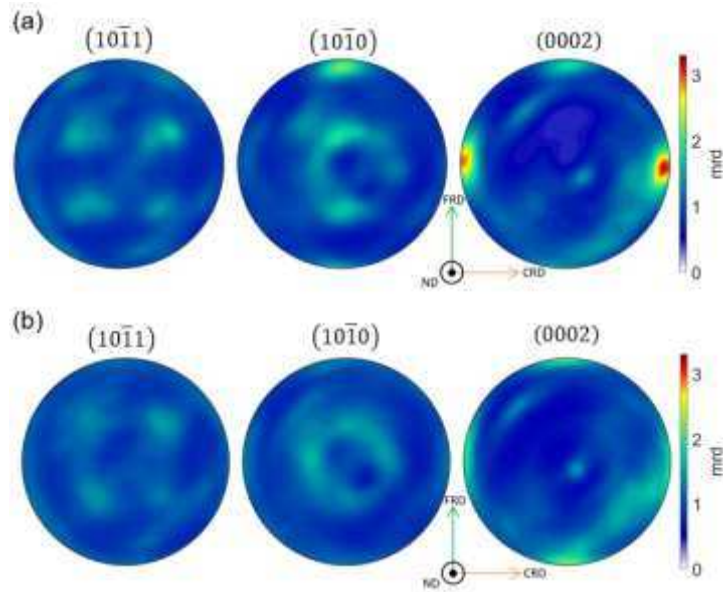


Figure 9 - ODF pole figure for the as-received material at a depth of (a) 0.5 mm and (b) 2 mm. (single column)

The pole figure for machined sample 7, Figure 10 (a), shows that the material in the white layer exhibits a strong basal  $\alpha(0002)$  texture. This is supported by a high multiples of random density (MRD) value, in the normal direction of the  $\alpha(0002)$  pole figure for sample 7, compared to the value near 1 for the as-received material in Figure 9 (a) and (b). MRD is a measure of the likelihood of finding a crystal in a certain orientation. By contrast, the swept grain region and a machined surface with no white layer both exhibit a shear texture, as presented in Figure 10 (b) and Figure 10 (c) respectively. It should be noted that the shear texture is towards the cutting direction for the swept grain region and away for a surface with good SI.

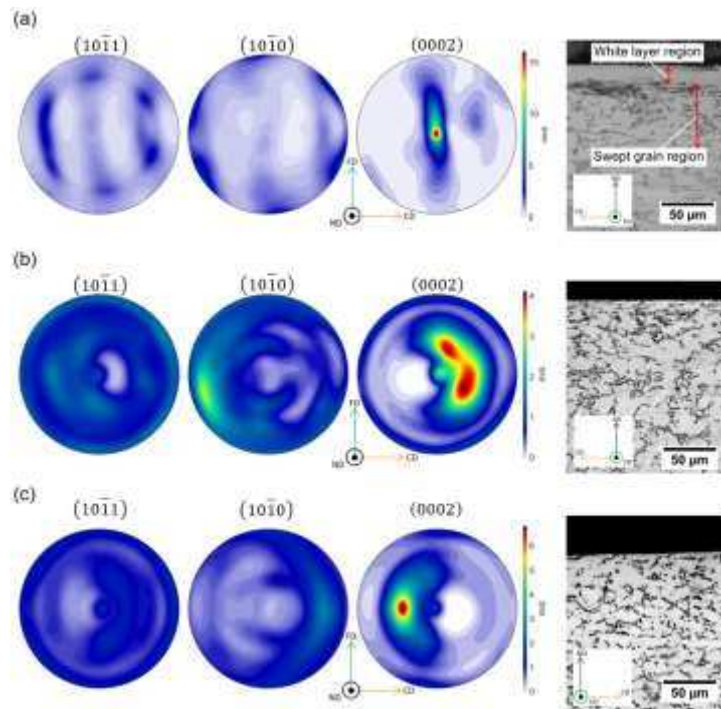


Figure 10 - ODF pole figures and corresponding micrographs: (a) machined sample 7 containing a white layer of up to 20  $\mu\text{m}$  in thickness, (b) a sample from trial 6 where the white layer has been removed to leave only the swept grain material and (c) a sample from trial 4 where no white layer was present. FD=feed direction, CD=cutting direction, ND=normal direction. (single column)

The compression texture in the white layer is supported by the cutting forces measured during machining with worn inserts, as shown in Figure 11 (a). The compressive (z) force of the tool on the workpiece (in the normal direction) was more than twice as large as the cutting and radial forces.

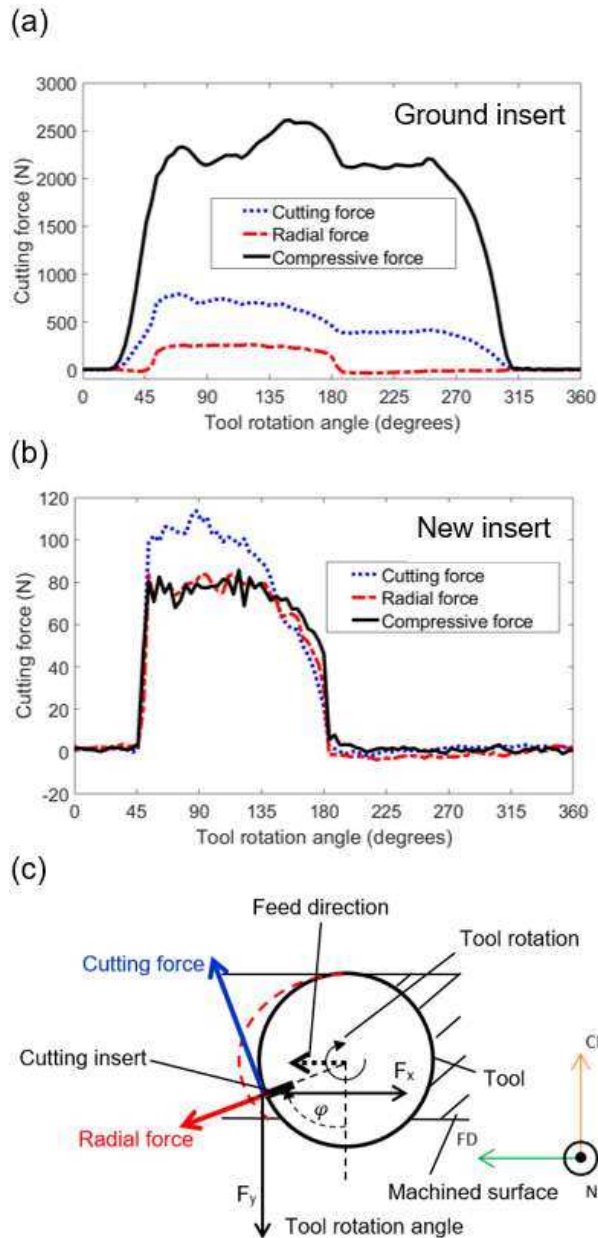


Figure 11 – Plots of the forces during one tool rotation: (a) sample 8 in which a white layer was generated on the surface and (b) sample 4, where a surface with good SI was produced. (c) A schematic outlining the coordinate system showing cutting and radial forces with respect to the x and y forces measured by the dynamometer. (single column)

A machined surface with good SI does not exhibit a compressive texture because the compressive loading during machining with new inserts was as much as 30 times smaller than for worn inserts, as shown in Figure 11 (b). The swept grain sample also lacks a compressive texture as, beneath the white layer, shear deformation was

dominant. This is evidenced by the grain distortion visible in the optical micrographs of the sub-surface, shown in Figure 10 (a) and (b), in which the residual  $\beta$ -grains are almost parallel to the surface, immediately below the white layer.

The texture changes due to machining, as presented in Table 2, become quantifiable through the calculation of the texture index (TI) for each surface. The TI is the square integral of the ODF for a pole figure, as such, it is a numerical indicator of preferential crystallographic orientation in a material. A larger TI indicates a stronger texture. It can be seen that all samples in which a white layer is present display a more ordered crystallographic structure than samples with no white layer at the surface.

Table 2 – TI and the key surface integrity features of each sample examined with XRD. (single column)

Sample	Texture index	Texture type	White layer thickness	Swept grain depth
Unmachined (0.5 mm)	1.31	Cross-rolled	0	0
Unmachined (2 mm)	1.18	Cross-rolled	0	0
2	2.13	Shear	0	5 $\mu\text{m}$
3	1.84	Shear	0	5 $\mu\text{m}$
4	2.14	Shear	0	5 $\mu\text{m}$
5	2.40	Compression	8 $\mu\text{m}$	72
6	2.60	Compression	10 $\mu\text{m}$	85 $\mu\text{m}$
6 swept grain	2.12	Shear	0	60 $\mu\text{m}$
7	4.12	Compression	8 $\mu\text{m}$	59 $\mu\text{m}$
7 swept grain	1.52	Shear	0	51 $\mu\text{m}$
8	3.42	Compression	16 $\mu\text{m}$	78 $\mu\text{m}$

To investigate the potential for a more targeted and rapid measurement of machined surface texture than is possible from pole figure measurements, X-ray intensity measurements in the phase analysis configuration were carried out for diffraction angles around the  $\alpha(0002)$  and  $\alpha(10\bar{1}1)$  peaks. It was found that the intensity ratio (IR) of the

$\alpha(0002)$  and  $\alpha(10\bar{1}1)$  peaks could be used to differentiate between samples with a white layer and those without, as shown in Figure 12. The IR was 8 times larger for a surface with a white layer than one without. To measure the data required to calculate the intensity ratio took 2 minutes, which is considerably faster than the 11 hours required to obtain pole figure data for a single sample.

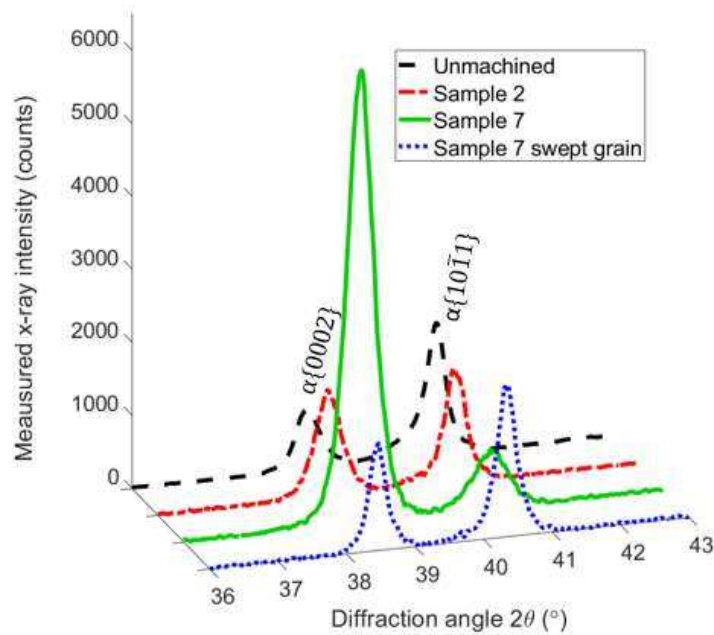


Figure 12 – Diffraction patterns from XRD reflection measurements on machined surface samples focusing on the  $\alpha(0002)$  and  $\alpha(10\bar{1}1)$  planes. (single column)

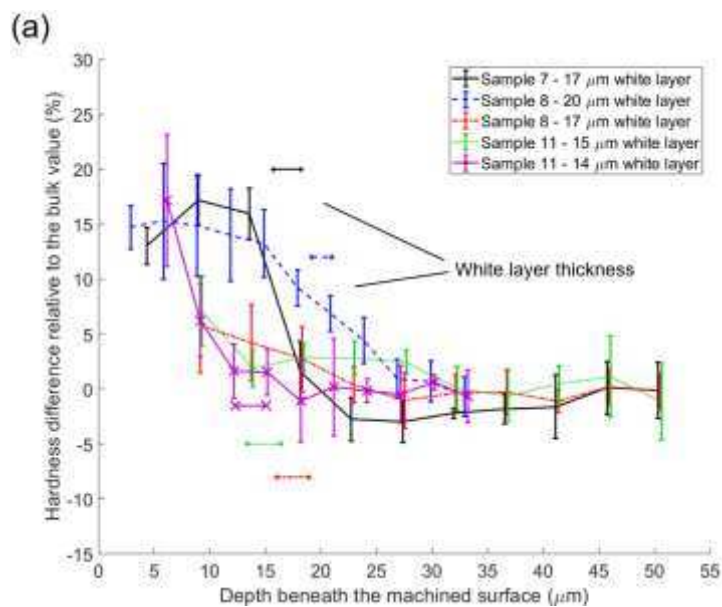
Sample	Intensity ratio
Unmachined	0.51
2 - No white layer	0.93
7 - 8 $\mu\text{m}$ white layer	7.60
7 swept grain – No white layer	0.71

Table 3 – The intensity ratio of the two XRD peaks for each machined surface. (single column)

### 3.4 Hardness and elastic modulus of the white layer

Nanoindentation was used to obtain hardness and elastic modulus profiles of cross-sectional samples, as shown in Figure 13 and Figure 14 respectively, as well as to investigate the effects of crystallographic orientation on the properties of the white

layer, as shown in Figure 15. The white layer was measured to be up to 15% harder than the bulk material in the cross-section, whereas there was no observable trend in hardness with increasing depth beneath the machined surface in samples without a white layer. Conversely, it was found that the elastic modulus increases with depth beneath the machined surface for the majority of samples with a white layer. The samples without a white layer show greater levels of uncertainty in the measured hardness value (6.8%) compared with those with a white layer (3.4%). It can be seen from Figure 15 that there is a 20-30% higher hardness value measured when indenting on top of the white layer compared to in the cross-section, as outlined in Figure 5.



(b)

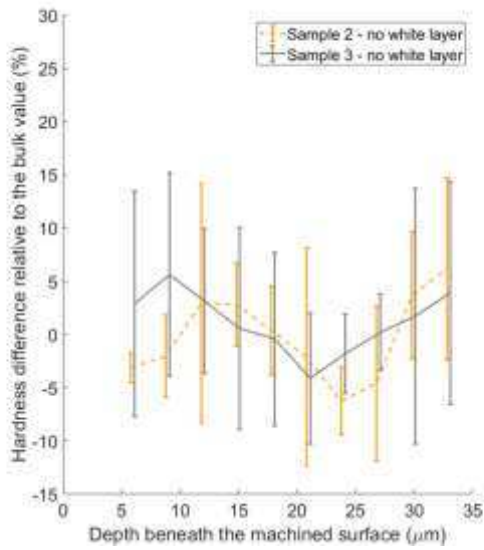
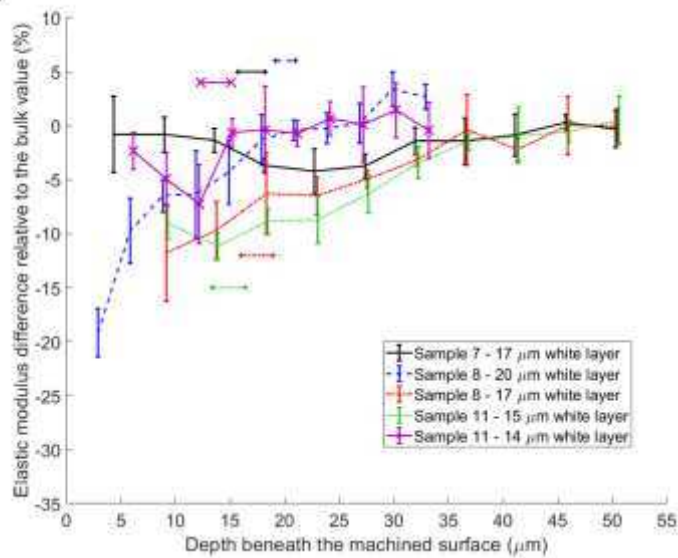


Figure 13 – Hardness measurements (relative to the bulk value) with depth in the cross-section of the machined surface: (a) surfaces with a white layer and (b) surfaces without a white layer. Error bars represent one standard deviation. The straight horizontal lines correspond to the white layer thickness for each surface, measured through optical microscopy near the nanoindentation array. The length of these lines defines  $\pm$  one standard deviation of the thickness measurement. (single column)

(a)



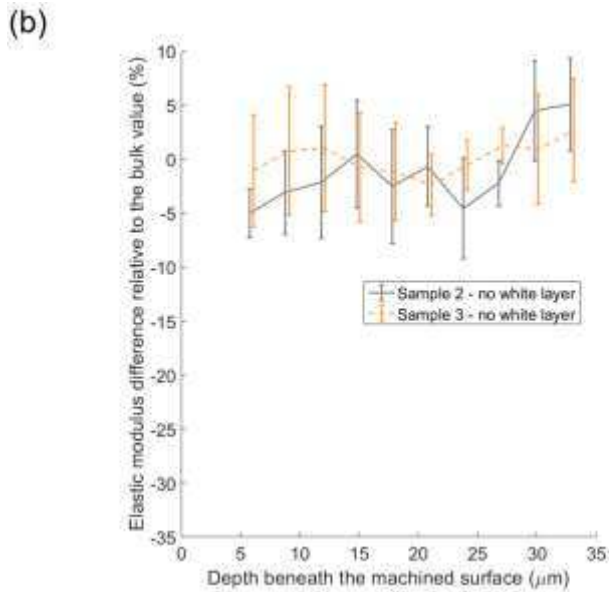


Figure 14 –Calculated elastic modulus (relative to the bulk value), with depth in the cross-section: (a) samples with a white layer and (b) samples without a white layer. (single column)

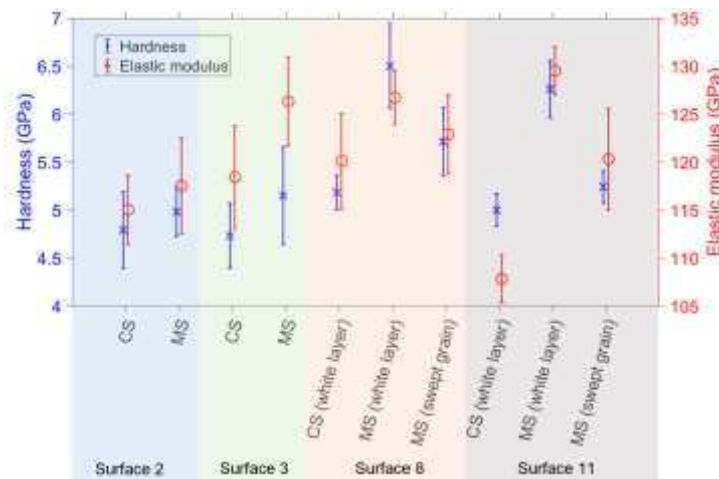


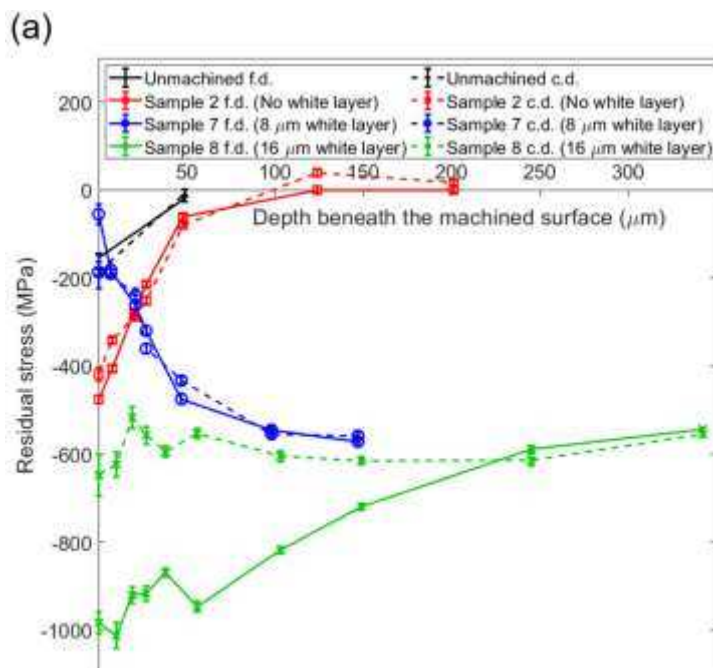
Figure 15 – Hardness and elastic modulus results from nanoindentation measurements of machined surface (MS) and cross-section (CS) samples. (single column)

### 3.5 Residual stress profiles

XRD Residual stress and corresponding peak broadening variations with increasing depth beneath the machined surface are shown in Figure 16 for the feed direction (solid lines) and cutting direction (dashed lines), as defined in Figure 3. A compressive surface residual stress state was measured for all samples tested,

including the as-received material. However, it is evident that despite samples 7 and 8 (plotted with o and x markers respectively) both containing a white layer at the surface, the near-surface residual stress for sample 8 is considerably more compressive. Both samples possess significant compressive stresses at depths up to 300  $\mu\text{m}$  beneath the surface that cannot be directly correlated to the observed white layers as they are less than 20 $\mu\text{m}$  thick for both surfaces. The sub-surface residual stress state is simply a consequence of the abusive machining carried out to generate the white layer, supported by the large forces measured during cutting, such as those presented in Figure 11 (a).

Peak broadening results for the same set of measurements are shown in Figure 16 (b). It can be seen that the peak broadening is greater, at all depths, for those samples with a white layer. At the machined surface, however, sample 2 (plotted with square markers), which has no white layer also has peak broadening that quickly reduces at greater depth to values closer to the unmachined material.



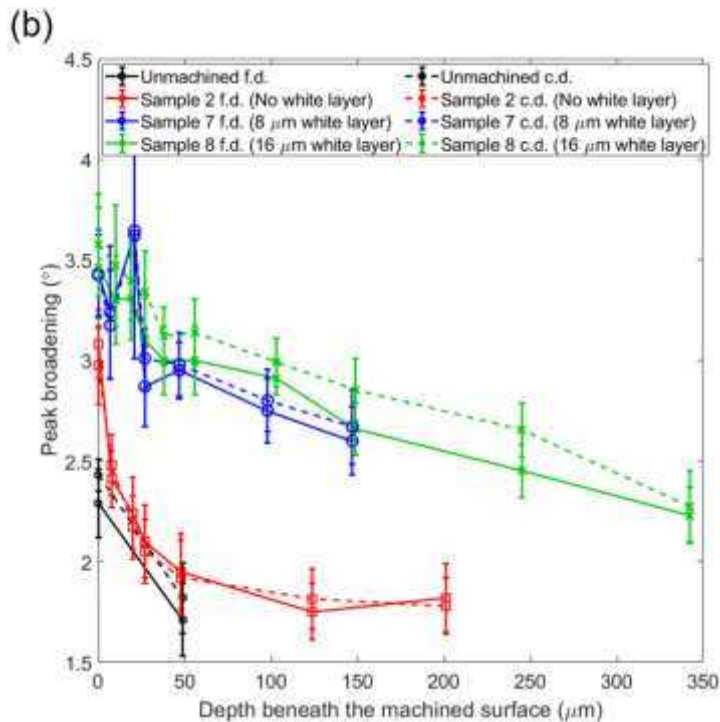


Figure 16 – (a) Residual stress profiles and (b) corresponding peak broadening values beneath the machined surface in the feed direction (f.d., indicated by the solid lines) and the perpendicular, cutting direction (c.d., indicated by the dashed lines). (single column)

## 4 Discussion

### 4.1.1 Key physical properties of the white layer

The results from destructive characterization indicate that white layers in titanium, formed by machining with worn inserts, possess a strong basal crystallographic texture, are composed of ultra-fine grains, are hardened relative to the bulk material and can exhibit different surface residual stress states.

The basal texture of the white layers generated with worn tools in this study is attributed to the large compressive forces during cutting which result from the high pressure applied by the machining centre to keep the cutting insert at the desired depth of cut, in combination with the large contact area of the ground inserts.

Lebensohn and Tomé [43] showed, through modelling, that the c-axis of the HCP crystal re-orientates under compression towards the axis of loading, therefore

indicating that the texture in the white layer is dominated by compression. This large compressive force at high levels of wear is not only seen when milling with artificially worn, ground inserts but has also been observed by Zhang et al. [44] when milling IN-718 and Chou and Evans [3] when hard turning steel, both with naturally worn inserts. Chou and Evans [3] specifically identified that a higher compressive force accompanies white layer formation.

The texture in the swept grain region, as well as surfaces with good surface integrity, is characteristic of the shear deformation that is visible in optical micrographs of these samples and has been observed elsewhere in the literature. Sagapuram et al. [45], for example, have reported a similar shear texture in magnesium, another hcp metal, after large strain extrusion machining. Beausir et al. [46] attributed basal pole rotation under macroscopic shear loading to the alignment of the basal planes of the HCP crystal with the shear plane, facilitating deformation via basal slip.

The different direction of the shear texture, relative to the cutting direction, in a sample with good surface integrity and a swept grain sample, where the white layer has been removed, can be attributed to the nature of the cutting operation when using a worn insert. When machining with a worn insert there is additional rubbing, without chip formation, during the second half of the tool rotation, as highlighted in Figure 17 and evident from the cutting force profile in Figure 11 (a). By contrast, with a new insert, there is only cutting with chip formation in the first half of the tool rotation and no rubbing. Thus, the final tool pass direction that deforms the workpiece surface for a worn insert is in the opposite direction than that for a new insert, when considering the central region of the machined shoulder width, resulting in a different texture direction.

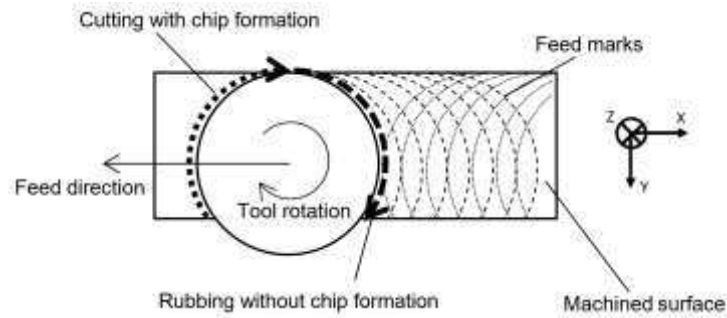


Figure 17 – Schematic indicating the key regions of the tool rotation responsible for the difference in shear textures. (single column)

Due to the  $\alpha + \beta$  microstructure of the as-received material, a higher concentration of retained- $\beta$  and or  $\alpha''$  would be expected in the case of phase transformation under high temperatures during white layer formation, as observed in titanium chips by Wan et al. [24]. These  $\alpha \rightarrow \beta$  and  $\beta \rightarrow \alpha''$  transformations would be observable through XRD measurements, however, it can be seen from the XRD patterns shown in Figure 8 that there was no significant  $\beta$  or  $\alpha''$  transformation. Therefore, white layer formation at low speeds and high levels of wear does not involve a temperature-induced phase transformation.

The SEM micrographs in Figure 6 and Figure 7 show that the white layer contains ultra-fine grains, smaller than 200 nm. Ultra-fine grain sizes in the white layer have been reported in hard turned steels by Barry and Byrne [16] and in a nickel superalloy by Herbert et al. [6], as such the comparable observation in titanium is not surprising. Similarly, increased hardness for the white layer region has been measured by Wusatowska-Sarnek et al. [19] for a nickel superalloy and by Akcan et al. [4] in steel. However, the values reported in these studies showed an increase, relative to the bulk, by as much as 60% and 25% respectively, both larger than the 15% change measured in this study for titanium. Wusatowska-Sarnek et al. [19] also reported a lower elastic modulus of the white layer in the cross-section, this was

attributed to grain refinement. Kim and Bush [47], identified that elastic modulus reduction due to grain refinement is only significant for grain sizes below 10 nm in a material with nano-scale grains, as such the reduction for titanium cannot be solely due to this mechanism. Instead, the lower elastic modulus is thought to be due to indentation into the prismatic plane in a cross-sectional sample, due to the strong texture of the white layer. Britton et al. [48] showed indentation in this plane produces lower measured values.

The true hardness change in the white layer due to grain refinement and strain hardening is difficult to attain due to the additional effect of crystallographic orientation. Rugg et al. [49], and Moussaoui et al. [50] have shown that hardness values, measured through nanoindentation in titanium, can vary by as much as 30-40% between grains of different orientations and different phases respectively. Indentation into the basal orientation can result in nanohardness values up to 30% higher than for indentation in the prismatic plane. Thus, when indenting in the cross-section of the white layer, which corresponds to indentation into the prismatic plane of the HCP crystal in most cases, due to the strong texture of this region, the hardness would be expected to be reduced, relative to an indentation on a machined surface sample. This is the result obtained in the nanoindentation measurements shown in Figure 15. The higher hardness for the white layer relative to the bulk material in cross-sectional samples must, therefore, be due to a combination of work hardening and grain refinement, which more than offsets the reduced hardness of the prismatic orientation.

The contrasting near-surface residual stress states for the two samples with white layers shows that white layers in titanium cannot be associated with a particular residual stress state. This difference in residual stress must be a consequence of the

different the thermomechanical loads imparted on the surface by machining at the particular combination of cutting parameters and tool conditions used to generate the surfaces. Surface 7, which contains a smaller compressive residual stress at the surface, was machined at 80 m/min, compared to 40 m/min for surface 8. Higher cutting speeds result in a greater rate of heat generation due to the higher strain rates imposed and this can encourage a more tensile residual stress, as shown by Velásquez et al. [31]. However, despite the different thermomechanical loads experienced, the same metallurgical change, white layer formation, was observed. At depths greater than 50  $\mu\text{m}$ , both surfaces with a white layer have significantly greater compressive residual stresses than the surfaces with no white layer due to the enhanced plastic deformation when cutting with worn inserts.

It should be noted that both samples with white layers showed increased peak broadening relative to the other samples. Ungár [51] showed that XRD peak broadening is caused by a reduction in grain size and lattice distortions, such as those caused by an increase in dislocation density. The small grain size of the white layer region has been shown in Figure 6 (b) and (c), and an increase in dislocation density is expected in the swept grain region due to SPD.

It is apparent, for the surfaces with a white layer, that the effect of machining on the workpiece extends far beyond the swept grain region. This is because peak broadening and residual stress values are still different from their baseline values of approximately  $1.75^\circ$  and 0 MPa, respectively, even at a depth of 350  $\mu\text{m}$ .

#### 4.2 The formation mechanism for white layers in titanium

As highlighted in the previous section, the basal texture measured in samples with a white layer is indicative of compression acting normal to the machined surface.

Fitzner et al. [52] have shown that reorientation of the HCP crystal under compression is due to activation of the  $\{10\bar{1}2\}$  tensile twinning mode which involves  $85^\circ$  pole rotation. Follansbee and Gray [53] have observed that twinning, rather than slip, is the dominant mechanism during compression at high strain rates and low temperatures. The extremely high strain rates experienced during machining when compared to other production processes, as outlined by Jaspers and Dautzenberg [54], can therefore activate twinning as the dominant deformation mechanism. This is despite the high temperatures that could be experienced during machining of titanium. Due to the  $85^\circ$  rotation in  $\{10\bar{1}2\}$  tensile twinning in addition to the largely random pole orientation prior to machining, for this mechanism to occur there must be activation of other slip or twinning systems before final  $\{10\bar{1}2\}$  twinning for a proportion of the grains. The prior crystallographic orientation of the structure, as shown in Figure 18 (a), dictates which specific systems drive the re-orientation of a particular grain, as highlighted by Bridier et al. [55]. Grains have a preference to re-orientate in such a way that develops the most stable condition with respect to a particular stress state, which, for HCP lattice under compression, gives rise to a basal texture. Therefore, in this case of white layer formation, the large-scale re-orientation of the HCP crystals occurs, depending on the prior orientation, either by  $\{10\bar{1}2\}$  twinning as shown in Figure 18 (b) or via initial slip and twinning mechanisms followed by final activation of the  $\{10\bar{1}2\}$  twinning mechanism, as shown in Figure 18 (c). This results in the basal texture presented in Figure 18 (d).

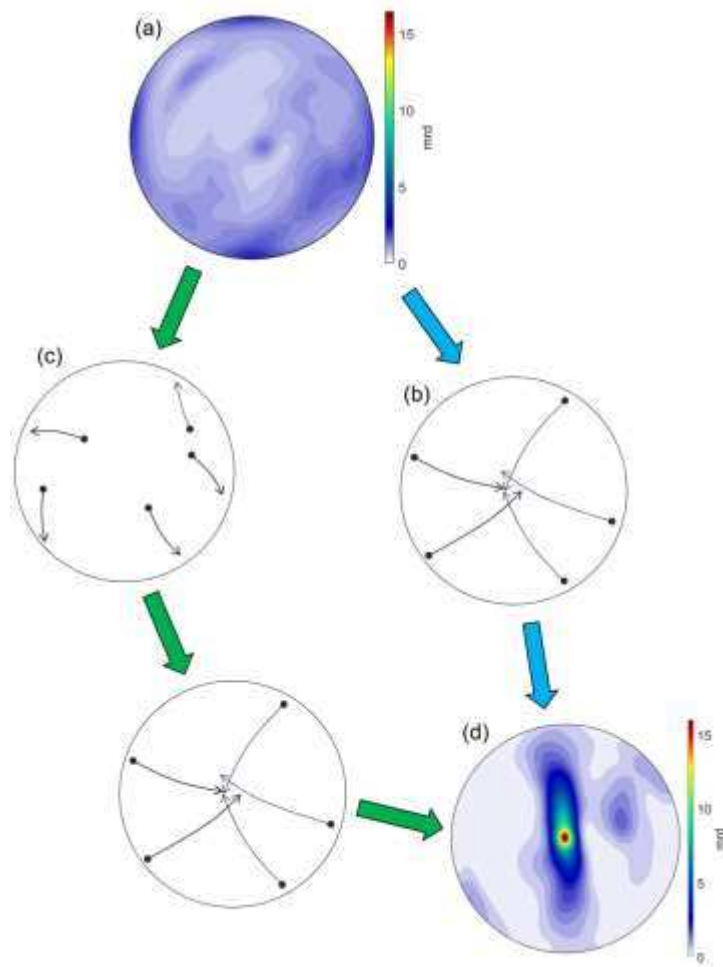


Figure 18 – Schematic outlining the possible routes to a basal texture from the starting workpiece texture: (a) (0002) Pole figure for the as-received material. (b) Basal pole rotation during  $\{10\bar{1}2\}$  tensile twinning. (c) Basal pole rotation in which the specific slip or twinning system involved depends on prior orientation followed by  $\{10\bar{1}2\}$  tensile twinning. (d) The basal texture in the white layer. (single column)

The lack of a temperature-dependent  $\alpha \rightarrow \beta$  phase transformation in the white layer, visible from XRD phase analysis, in addition to the distorted microstructure immediately beneath the white layer, in Figure 4 (a), indicates that SPD could be responsible for the observed grain refinement. The material in the white layer region is experiencing high temperatures and large forces over a very short time during machining, therefore, a form of recrystallization may have occurred to generate the

fine microstructure shown in Figure 6 (b). Considering the duration of the events during machining, this is anticipated to be dynamic recrystallization (DRX).

This proposed mechanism for recrystallization is aligned with results reported by Derby [56] that both discontinuous (migrational) DRX and continuous (rotational) DRX can occur under conditions of large strain and high temperature. Meyers et al. [57] also showed that at high strain rates, such as those that can be imposed during machining operations, continuous DRX (CDRX) prevails over discontinuous DRX (DDRX) due to the short time at high temperature. Sakai et al. [58] reported that the texture resulting from CDRX is typically representative of the deformation i.e. the deformation has little effect on the texture, whereas in DDRX the deformation texture is weakened.

The resulting crystallographic texture of the white layers formed by machining with worn tools is a strong compressive deformation texture, as shown in Figure 10 (a), rather than a recrystallization texture. This is in addition to the notion that the white layer was formed at high strain rates as a consequence of being machined.

Therefore, it is believed that continuous dynamic recrystallization (CDRX), as described by Wang and Huang [59], has occurred in the generation of the microstructure of the white layer and the immediately adjacent region of swept grain. The limited time at high temperature restricts grain growth such that the grains within the newly formed white layer are as much as 100 times smaller than the bulk material grain size.

It is apparent that the mechanism of white layer formation when using worn inserts at low speeds, as presented in this study, is different in a number of ways from that proposed by Xu et al. [22]. When using worn tools and low speeds, there was no precipitation of the  $\beta$ -phase, indicating that temperature and strain rates were not as

high compared to HSM. It was also identified the  $\{10\bar{1}2\}$  twinning mode is more dominant when machining with worn inserts, compared to the  $\{10\bar{1}1\}$  for HSM. However, CDRX is the mechanism attributed to grain refinement in both cases.

#### 4.3 The potential for non-destructive detection of white layers in titanium

It has been shown, in this paper, that XRD measurements can be used to distinguish between a surface with a white layer and a surface without. Specifically, there is a relative increase in the  $\alpha(0002)$  peak compared to the  $\alpha(10\bar{1}1)$  peak for a surface with a white layer, due to the resultant basal texture of this region. Additionally, XRD peak broadening was measured to be greater when a white layer was present on the surface of a sample. Therefore, it may be possible to detect white layers in titanium alloys non-destructively using XRD peak intensity ratio or peak broadening analysis of machined surfaces. In principle, XRD is a non-destructive method, however, in practice, the technique has limitations as large samples typically need to be cut into smaller sections to fit in a machine for analysis. Portable systems which remove sample size restrictions, such as that developed by Uda [60], may facilitate truly non-destructive XRD for white layer detection.

Brown et al. [29] have identified that surface acoustic wave (SAW) testing may also facilitate non-destructive detection of white layers via the effects of grain size and crystallographic textures on the propagation of SAWs. This is because the velocity of a SAW wave propagating on the basal plane of the HCP crystal is high in all directions on this plane compared with other crystallographic orientations, according to Farnell [61]. Additionally, Li et al. [62] identified that the attenuation of SAWs was enhanced at smaller grain sizes.

As a consequence of the nano-grains present in the white layer and immediately beneath in the swept grain region, there may be increased attenuation of a SAW on a machined surface with poor surface integrity. Additionally, due to the basal texture of white layers, there should be high SAW propagation velocity in all measurement directions. By contrast, on a surface without a white layer, propagation would be on a more random combination of planes and as such, propagation velocity should be slower and would vary depending on the propagation direction. Therefore, a detection method based on SAWs could permit non-destructive detection of white layers on actual industrial parts manufactured from Ti-alloys.

## 5 Conclusions

This research was conducted to determine the key properties of white layers formed in the machining of Ti-6Al-4V to identify potential techniques to detect this SI feature non-destructively. This study is the first of its kind that evaluates applications of various characterization methods and reports a quantitative comparison of the findings. The main conclusions of this work can be summarized as below:

- Machining induced white layers in Ti-6Al-4V have a basal texture because of the compressive stress state imposed during machining with worn inserts.
- White layers in titanium, formed under the applied machining conditions, are composed of ultra-fine equiaxed grains with an average diameter of less than 200 nm.
- XRD phase analysis suggests that the white layers observed in this study did not form via an  $\alpha \rightarrow \beta$  phase transformation mechanism.

- The white layer is up to 15% harder than the bulk material and has a lower elastic modulus relative to the bulk material.
- Residual stress profiles beneath the machined surface have shown there is no single residual stress state that can be associated with the presence of a white layer.
- It has been proposed that white layers in Ti-6Al-4V are formed by continuous dynamic recrystallization driven by severe plastic deformation under the high strain rates experienced during metal cutting.
- Results indicate that white layers in titanium could be detected through XRD measurements, due to the strong basal texture and small grain size of the white layer.
- Due to the anisotropy of mechanical properties caused by HCP orientation, it is predicted white layers in Ti-6Al-4V may be detected non-destructively using SAWs, through change in wave propagation velocity caused by crystallographic texture.

### **Acknowledgements**

This research was supported by Rolls-Royce and Seco Tools in addition to the EPSRC [grant number EP/L016257/1]

### **Data availability**

The raw/processed data required to reproduce these findings cannot be shared at this time as the data also forms part of an ongoing study.

### **References**

- [1] W.P. Koster, M. Field, J.F. Kahles, L.J. Fritz, L.R. Gatto, Surface integrity of machined structural components, Metcut research associates inc Cincinnati OH, 1970.
- [2] Rolls-Royce, Inspection standard, Unpublished results.
- [3] Y.L. Chou, C.J. Evans, White layers and thermal modeling of hard turned surfaces, *International Journal of Machine Tools & Manufacture* 39 (1999) 1863-1881.
- [4] S. Akcan, W.S. Shah, S.P. Moylan, S. Chandrasekar, P.N. Chhabra, H.T.Y. Yang, Formation of white layers in steels by machining and their characteristics, *Metallurgical and Materials Transactions A* 33(4) (2002) 1245-1254.
- [5] W.P. Koster, M. Field, J.B. Kohls, L.J. Fritz, L.R. Gatto, Manufacturing Methods for Surface Integrity Machined Structural Components, Technical Report (1972) 86-115.
- [6] C.R.J. Herbert, D.A. Axinte, M.C. Hardy, P.D. Brown, Investigation into the Characteristics of White Layers Produced in a Nickel-Based Superalloy from Drilling Operations, *Procedia Engineering* 19 (2011) 138-143.
- [7] A. Ramesh, S.N. Melkote, L.F. Allard, L. Riester, T.R. Watkins, Analysis of white layers formed in hard turning of AISI 52100 steel, *Materials Science and Engineering: A* 390(1–2) (2005) 88-97.
- [8] Y. Guo, J. Sahni, A comparative study of hard turned and cylindrically ground white layers, *International Journal of Machine Tools and Manufacture* 44(2-3) (2004) 135-145.
- [9] Z. Chen, M.H. Colliander, G. Sundell, R.L. Peng, J. Zhou, S. Johansson, J. Moverare, Nano-scale characterization of white layer in broached Inconel 718, *Materials Science and Engineering: A* 684 (2017) 373-384.
- [10] S.B. Hosseini, U. Klement, J. Kaminski, Microstructure characterization of white layer formed by hard turning and wire electric discharge machining in high carbon steel (AISI 52100), *Advanced Materials Research* 409 (2012) 684-689.
- [11] W. Lojkowski, M. Djahanbakhsh, G. Bürkle, S. Gierlotka, W. Zielinski, H.J. Fecht, Nanostructure formation on the surface of railway tracks, *Materials Science and Engineering: A* 303(1) (2001) 197-208.
- [12] H.C. Rogers, Adiabatic plastic deformation, *Annual Review of Materials Science* 9(1) (1979) 283-311.
- [13] B. Zhang, W. Shen, Y. Liu, X. Tang, Y. Wang, Microstructures of surface white layer and internal white adiabatic shear band, *Wear* 211(2) (1997) 164-168.
- [14] G. Poulachon, A. Albert, M. Schluraff, I.S. Jawahir, An experimental investigation of work material microstructure effects on white layer formation in PCBN hard turning, *International Journal of Machine Tools and Manufacture* 45(2) (2005) 211-218.
- [15] K.D. Edkins, N.J.v. Rensburg, R.F. Laubscher, Evaluating the Subsurface Microstructure of Machined Ti-6Al-4V, *Procedia CIRP* vol. 13 (2014) pp. 270-275.
- [16] J. Barry, G. Byrne, TEM study on the surface white layer in two turned hardened steels, *Materials Science and Engineering: A* 325(1–2) (2002) 356-364.
- [17] S. Smith, S.N. Melkote, E. Lara-Curzio, T.R. Watkins, L. Allard, L. Riester, Effect of surface integrity of hard turned AISI 52100 steel on fatigue performance, *Materials Science and Engineering: A* 459(1–2) (2007) 337-346.
- [18] C. Herbert, D.A. Axinte, M. Hardy, P. Withers, Influence of Surface Anomalies Following Hole Making Operations on the Fatigue Performance for a Nickel-Based Superalloy, *Journal of Manufacturing Science and Engineering* 136(5) (2014) 051016 1-9.
- [19] A.M. Wusatowska-Sarnek, B. Dubiel, A. Czyska-Filemonowicz, P.R. Bhowal, N. Ben Salah, J.E. Klemberg-Sapieha, Microstructural Characterization of the White Etching Layer in Nickel-Based Superalloy, *Metallurgical and Materials Transactions A* 42(12) (2011) 3813-3825.
- [20] B.J. Griffiths, Mechanisms of White Layer Generation With Reference to Machining and Deformation Processes, *Journal of Tribology* 109(3) (1987) 525-530.
- [21] S.B. Hosseini, U. Klement, Y. Yao, K. Rytberg, Formation mechanisms of white layers induced by hard turning of AISI 52100 steel, *Acta Materialia* 89 (2015) 258-267.

- [22] X. Xu, J. Zhang, H. Liu, Y. He, W. Zhao, Grain refinement mechanism under high strain-rate deformation in machined surface during high speed machining Ti6Al4V, *Materials Science and Engineering: A* (2019).
- [23] C.R.J. Herbert, J. Kwong, M.C. Kong, D.A. Axinte, M.C. Hardy, P.J. Withers, An evaluation of the evolution of workpiece surface integrity in hole making operations for a nickel-based superalloy, *Journal of Materials Processing Technology* 212(8) (2012) 1723-1730.
- [24] Z. Wan, Y. Zhu, H. Liu, Y. Tang, Microstructure evolution of adiabatic shear bands and mechanisms of saw-tooth chip formation in machining Ti6Al4V, *Materials Science and Engineering: A* 531 (2012) 155-163.
- [25] V. Bushlya, J.M. Zhou, F. Lenrick, P. Avdovic, J.E. Ståhl, Characterization of White Layer Generated when Turning Aged Inconel 718, *Procedia Engineering* 19 (2011) 60-66.
- [26] J.M. Zhou, V. Bushlya, R.L. Peng, S. Johansson, P. Avdovic, J.E. Stahl, Effects of Tool Wear on Subsurface Deformation of Nickel-based Superalloy, *Procedia Engineering* 19 (2011) 407-413.
- [27] Z. Fang-yuan, D. Chun-zheng, X. Xin-xin, W. Min-jie, Influence of cutting condition on white layer induced by high speed machining of hardened steel, *The International Journal of Advanced Manufacturing Technology* (2017) 77-84.
- [28] N. Fang, Q. Wu, A comparative study of the cutting forces in high speed machining of Ti-6Al-4V and Inconel 718 with a round cutting edge tool, *Journal of materials processing technology* 209(9) (2009) 4385-4389.
- [29] M. Brown, D. Wright, R. M'Saoubi, J. McGourlay, M. Wallis, A. Mantle, P. Crawforth, H. Ghadbeigi, Destructive and non-destructive testing methods for characterization and detection of machining-induced white layer: A review paper, *CIRP Journal of Manufacturing Science and Technology* (2018).
- [30] J. Schindelin, I. Arganda-Carreras, E. Frise, V. Kaynig, M. Longair, T. Pietzsch, S. Preibisch, C. Rueden, S. Saalfeld, B. Schmid, Fiji: an open-source platform for biological-image analysis, *Nature methods* 9(7) (2012) 676.
- [31] J.D.P. Velásquez, A. Tidu, B. Bolle, P. Chevrier, J.J. Fundenberger, Sub-surface and surface analysis of high speed machined Ti-6Al-4V alloy, *Materials Science and Engineering: A* 527(10-11) (2010) 2572-2578.
- [32] W.C. Oliver, G.M. Pharr, An improved technique for determining hardness and elastic modulus using load and displacement sensing indentation experiments, *Journal of materials research* 7(06) (1992) 1564-1583.
- [33] ASTM, E384: Standard Test Method for Knoop and Vickers Hardness of Materials, 2012, pp. 1-43.
- [34] G. Welsch, R. Boyer, E. Collings, *Materials properties handbook: titanium alloys*, ASM international first edition (1993) 494-497.
- [35] AbsorbDX 1.1 DIFFRACplus, Bruker AXS GmbH, Karlsruhe, Germany, 2004.
- [36] PDF-4+ Sleve+, ICDD, PA 19073, USA, 2018.
- [37] PDF-4+ 2019, International Centre for Diffraction Data, Newtown Square, PA, USA, 2018.
- [38] F. Bachmann, R. Hielscher, H. Schaeben, Texture analysis with MTEX-free and open source software toolbox, *Solid State Phenomena, Trans Tech Publ*, 2010, pp. 63-68.
- [39] B.D. Cullity, S.R. Stock, *Elements of X-ray Diffraction*, Prentice hall New Jersey 2001.
- [40] M. Fitzpatrick, A. Fry, P. Holdway, F. Kandil, J. Shackleton, L. Suominen, Determination of residual stresses by X-ray diffraction, *Measurement good practice guide*, 2005.
- [41] D.L. Sikarskie, A series form of correction to stresses measured using x-ray diffraction, *AIME MET SOC TRANS* 239(4) (1967) 577-580.
- [42] ASTM, E112-96 (2004) e2: Standard Test Methods for Determining Average Grain Size, 2004.
- [43] R.A. Lebensohn, C.N. Tomé, A self-consistent anisotropic approach for the simulation of plastic deformation and texture development of polycrystals: Application to zirconium alloys, *Acta Metallurgica et Materialia* 41(9) (1993) 2611-2624.

- [44] S. Zhang, J.F. Li, Y.W. Wang, Tool life and cutting forces in end milling Inconel 718 under dry and minimum quantity cooling lubrication cutting conditions, *Journal of Cleaner Production* 32 (2012) 81-87.
- [45] D. Sagapuram, M. Efe, W. Moscoso, S. Chandrasekar, K.P. Trumble, Controlling texture in magnesium alloy sheet by shear-based deformation processing, *Acta Materialia* 61(18) (2013) 6843-6856.
- [46] B. Beausir, L.S. Tóth, K.W. Neale, Ideal orientations and persistence characteristics of hexagonal close packed crystals in simple shear, *Acta Materialia* 55(8) (2007) 2695-2705.
- [47] H.S. Kim, M.B. Bush, The effects of grain size and porosity on the elastic modulus of nanocrystalline materials, *Nanostructured materials* 11(3) (1999) 361-367.
- [48] T.B. Britton, H. Liang, F. Dunne, A. Wilkinson, The effect of crystal orientation on the indentation response of commercially pure titanium: experiments and simulations, *Proceedings of the Royal Society of London A: Mathematical, Physical and Engineering Sciences*, The Royal Society, 2009, pp. 1-25.
- [49] D. Rugg, T.B. Britton, J. Gong, A.J. Wilkinson, P.A.J. Bagot, In-service materials support for safety critical applications – A case study of a high strength Ti-alloy using advanced experimental and modelling techniques, *Materials Science and Engineering: A* 599 (2014) 166-173.
- [50] K. Moussaoui, M. Mousseigne, J. Senatore, R. Chieragatti, F. Monies, Influence of milling on surface integrity of Ti6Al4V—study of the metallurgical characteristics: microstructure and microhardness, *The International Journal of Advanced Manufacturing Technology* 67(5) (2013) 1477-1489.
- [51] T. Ungár, Microstructural parameters from X-ray diffraction peak broadening, *Scripta Materialia* 51(8) (2004) 777-781.
- [52] A. Fitzner, D.L. Prakash, J.Q. da Fonseca, M. Thomas, S.-Y. Zhang, J. Kelleher, P. Manuel, M. Preuss, The effect of aluminium on twinning in binary alpha-titanium, *Acta Materialia* 103 (2016) 341-351.
- [53] P.S. Follansbee, G.T. Gray, An analysis of the low temperature, low and high strain-rate deformation of Ti–6Al–4V, *Metallurgical Transactions A* 20(5) (1989) 863-874.
- [54] S. Jaspers, J. Dautzenberg, Material behaviour in metal cutting: strains, strain rates and temperatures in chip formation, *Journal of materials processing technology* 121(1) (2002) 123-135.
- [55] F. Bridier, P. Villechaise, J. Mendez, Slip and fatigue crack formation processes in an  $\alpha/\beta$  titanium alloy in relation to crystallographic texture on different scales, *Acta Materialia* 56(15) (2008) 3951-3962.
- [56] B. Derby, The dependence of grain size on stress during dynamic recrystallisation, *Acta metallurgica et materialia* 39(5) (1991) 955-962.
- [57] M.A. Meyers, V.F. Nesterenko, J.C. LaSalvia, Q. Xue, Shear localization in dynamic deformation of materials: microstructural evolution and self-organization, *Materials Science and Engineering: A* 317(1-2) (2001) 204-225.
- [58] T. Sakai, A. Belyakov, R. Kaibyshev, H. Miura, J.J. Jonas, Dynamic and post-dynamic recrystallization under hot, cold and severe plastic deformation conditions, *Progress in materials science* 60 (2014) 130-207.
- [59] Y.N. Wang, J.C. Huang, Texture analysis in hexagonal materials, *Materials Chemistry and Physics* 81(1) (2003) 11-26.
- [60] M. Uda, In situ characterization of ancient plaster and pigments on tomb walls in Egypt using energy dispersive X-ray diffraction and fluorescence, *Nuclear Instruments and Methods in Physics Research Section B: Beam Interactions with Materials and Atoms* 226(1-2) (2004) 75-82.
- [61] G. Farnell, Properties of elastic surface waves, *Physical acoustics* 6 (1970) 109-166.
- [62] X. Li, Y. Song, F. Liu, H. Hu, P. Ni, Evaluation of mean grain size using the multi-scale ultrasonic attenuation coefficient, *NDT & E International* 72 (2015) 25-32.